ACS Energy LETTERS

http://pubs.acs.org/journal/aelccp

Tracking Local pH Dynamics during Water Electrolysis via In-Line Continuous Flow Raman Spectroscopy

Raul A. Marquez, Jay T. Bender, Shashwati C. da Cunha, Ashton M. Aleman, Amaresh Sahu, Venkat Ganesan, Delia J. Milliron, Joaquin Resasco, Thomas F. Jaramillo, and C. Buddie Mullins*

Cite This: ACS Energy Lett. 2025, 10, 2075−2083

Read Online

ACCESS | Metrics & More | Article Recommendations | Supporting Information

ABSTRACT: The performance of electrochemical devices, which play a critical role in decarbonization efforts, is often governed by proton-coupled electron transfer reactions at the electrode−electrolyte interface. These reactions are highly sensitive to the complex and dynamic microenvironment present at the electrode surface. However, characterizing this environment—particularly monitoring interfacial pH and its evolution under reaction conditions—remains challenging, necessitating the development of advanced analytical tools. Here, we introduce in-line continuous flow Raman spectroscopy (CFRS) as a spectroelectrochemical platform for quantifying interfacial pH swings generated during water-splitting. By monitoring phosphate ion speciation and controlling the hydrodynamics with a flow cell, we measure pH swings as a function of current density, flow rate, and distance from the electrode. Comparison with theoretical models reveals the impact of bulk pH, boundary layer thickness, and bubble dynamics at high current densities. Collectively, these findings establish CFRS as a platform for quantitatively investigating pH dynamics, offering critical insights for advancing electrochemical energy conversion technologies.

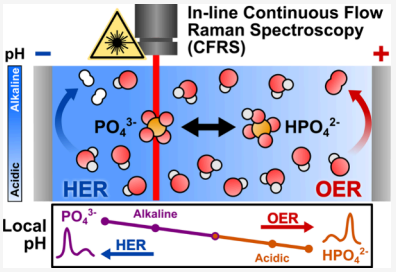

The highly complex and dynamic nature of electrochemical interfaces has deservedly gained substantial attention in recent years.[1,2] Building on significant efforts that have aimed at understanding how electrode structure and composition relate to performance, there has been an increased focus associated with understanding the critical role of the microenvironment at these complex interfaces. In heterogeneous electrocatalysis,[3] it is known that the conditions at the electrode surface strongly impact the rates of proton-coupled electron transfer (PCET) reactions in aqueous systems. These reactions underlie key electrocatalytic processes, including the hydrogen evolution reaction (HER), oxygen evolution reaction (OER), oxygen reduction reaction (ORR), and carbon dioxide reduction reaction (CO_2RR), among others.[4] Therefore, understanding the factors influencing PCET reactions not only advances our fundamental understanding of electrocatalysis but also furthers the development of critical electrochemical technologies like electrolyzers and fuel cells, which are pivotal for industrial decarbonization strategies.[3,5]

Among the many variables influencing PCET processes, the electrolyte pH plays a particularly important role. This measure of proton activity affects the activity, stability, and selectivity of electrocatalytic materials.[4,6,7] Changes in pH have been shown to influence the selectivity of the CO_2RR,[5,7,8] alter ORR kinetics,[9−11] and accelerate the corrosion of electrocatalysts.[12−14] However, it is essential to note that these surface processes respond to the interfacial pH at the electrode surface rather than the bulk pH.[4] Since PCET reactions consume or generate protons, pH variations can develop in a narrow region near the electrode surface. In this region, often referred to as a local or microenvironment, the proton activity can differ markedly from that of the bulk electrolyte. The magnitude of these pH swings depends on various spatial, chemical, and operational conditions, posing a challenge for precise characterization.

Quantifying interfacial pH is difficult due to the inherent complexity of electrochemical systems across multiple length scales, which influences mass and ion transport.[4] Additionally, from an industrial standpoint, operating conditions, such as high current densities, variable power, impure feedstocks, and concentrated electrolytes,[15−17] further complicate the task of

Received: February 23, 2025
Revised: March 30, 2025
Accepted: April 1, 2025

predicting the interfacial pH. This lack of accurate characterization impedes the rational optimization of state-of-the-art electrolyzers and their components.[18] While conventional methods have been reported,[4,5,7,8,10,19−25] there is still a need for real-time interfacial pH measurements using techniques compatible with industrially relevant conditions, such as high current densities, forced electrolyte flow, and practical electrolyzer architectures.[26,27] Analytical tools compatible with such environments would enable the study of unique phenomena influenced by interfacial pH, such as gradients in polymer overlayers,[4] catalyst corrosion,[28−30] growth and detachment of gas bubbles,[31] and ionomer/membrane degradation.[32] Developing such platforms will open new opportunities to study interfacial pH dynamics in more complex and realistic electrochemical systems.

Herein, we describe an analytical platform for in situ measurement of local pH using continuous flow Raman spectroscopy (CFRS). We demonstrate the utility of this technique by measuring pH swings during water-splitting reactions under alkaline and near-neutral conditions. A phosphate molecular probe (PMP) was employed to estimate local pH based on the relative intensity of Raman bands associated with protonated and deprotonated forms of phosphate. Measurements were conducted in real-time using an electrochemical flow cell operating at current densities up to 200 mA·cm^{-2}. By controlling the position of the Raman laser relative to the electrode surface, we were able to quantify local pH swings with micron-scale spatial resolution. Our in-line CFRS technique overcomes the limitations of previous pH sensing methods by providing real-time, high-resolution mapping of interfacial pH dynamics under more industrially relevant operating conditions. The measurements demonstrate, in a highly quantitative manner, the substantial interfacial pH variations present under near-neutral bulk conditions compared to the less-pronounced, but measurable interfacial changes observed for bulk alkaline conditions. Consistent with expectations, the magnitude of these pH variations depends on the applied current density and the thickness of the apparent boundary layer, which in turn depends on the flow rate through the cell. In an effort to gain deeper insights, we compare our observed measurements with theoretical interfacial pH models, revealing an unexpected finding: while the trends observed in both theory and experiment were similar, the magnitudes of the pH swings were not. Simulations predict intense pH swings at high current densities; however, our CFRS measurements reveal more moderate deviations. We attribute this difference to vigorous bubble generation at high currents, which enhances mixing near the electrode surface that can counteract interfacial pH gradients. Collectively, our findings show the importance of in situ/operando measurements at interfaces and that in-line CFRS provides a versatile platform for studying interfacial pH dynamics, especially under operating conditions that more closely resemble commercial systems. This technique enables more accurate understanding of pH-dependent processes at electrochemical interfaces and helps advance the design of next-generation electrochemical technologies.

IN-LINE CFRS MEASUREMENTS

Figure 1a shows the CFRS analytical platform, which features an electrochemical flow cell equipped with a visualization window, allowing a Raman microscope to collect information at varying distances from the electrode surface. The electrodes

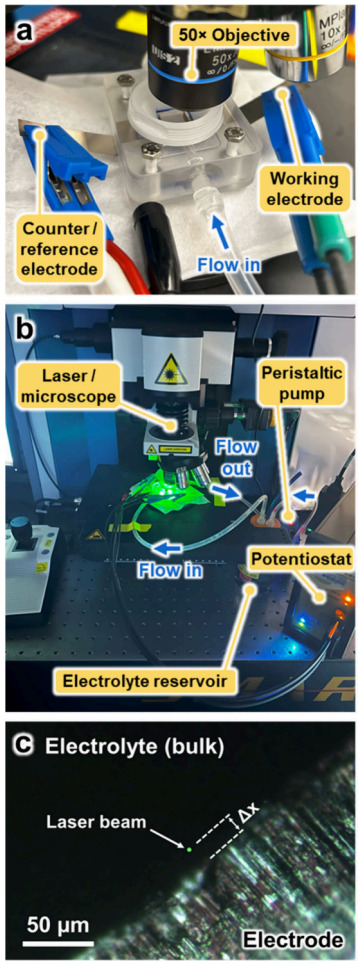

Figure 1. In-line CFRS enables local pH measurements in an electrochemical flow cell. (a) Photo of the electrochemical flow cell, (b) CFRS flow configuration during electrochemical measurements, and (c) Raman microscope image capturing the electrode−electrolyte interface and the laser beam located nominally 10 μm from the electrode surface (for this particular experiment). The white dashed lines indicate the distance the laser beam is from the electrode surface.

are aligned in parallel within a rectangular flow channel, with the electrolyte flowing perpendicular to the laser path. Detailed schematics and dimensions of the flow cell are provided in Figure S1 in the Supporting Information. The electrochemical flow cell operates in a two-electrode configuration under a constant current, with electrolyte recirculation maintained through a peristaltic pump (Figure 1b). Raman spectroscopy measurements are performed in-line, that is, directly within the flow cell as electrochemical reactions proceed, without the need to extract samples from the system. As shown in Figure 1c, the laser beam (with a spot size of ∼1.3 μm using a 532 nm green laser) can be positioned at a variable distance from the electrode surface (referred to as Δx) using the optical microscope, with the laser beam oriented parallel to the surface.

The mass transport properties of the flow cell were characterized using established protocols from the literature.[27,33,34] Here, boundary layer thicknesses were determined using the reduction of a facile redox couple (ferricyanide/ferrocyanide) under complete mass transport control at various flow rates (Figure S2). Specifically, at flow rates of 50 and 100

https://doi.org/10.1021/acsenergylett.5c00582
ACS Energy Lett. 2025, 10, 2075−2083

mL·min^{-1}, boundary layer thicknesses were estimated to be 40 and 30 μm, respectively (Figure S2e). A detailed description of this method and the interpretation of the apparent boundary layer is provided in the Supporting Information (Section S3).

Interfacial pH measurements were carried out under alkaline and near-neutral conditions using phosphate species as molecular probes. As phosphate undergoes acid−base equilibrium reactions, forming different protonated and deprotonated species depending on pH, the local pH can be estimated from the relative intensity of Raman bands associated with each form. Phosphate species are especially well-suited for this purpose due to the separability of the Raman bands produced by each species and the broad pH range over which this method can be applied.[35] We adhered to essential guidelines for using phosphate-based electrolytes in water-splitting reactions,[36] and used Pt foil electrodes to minimize contributions from parasitic redox processes.[4] In this work, we report measurements using 0.5 M phosphate molecular probe (PMP) electrolytes, free of chloride ions, operating under alkaline (PO_4^{3-}/HPO_4^{2-}, p$K_{a,3}$ = 12.36) and near-neutral ($HPO_4^{2-}/H_2PO_4^{-}$, p$K_{a,2}$ = 7.20) conditions. PMP electrolytes have been previously used for in situ local pH measurements,[35,37] however, our platform introduces three new advances: (1) a flow cell architecture that enables local pH measurements at controllable distances from the electrode surface, (2) operation at significantly higher current densities (up to 200 mA·cm^{-2}), and (3) controlled hydrodynamic conditions to investigate the influence of the apparent boundary layer.

HIGH CURRENT DENSITIES INTENSIFY LOCAL PH SWINGS

To investigate the effect of current density on the magnitude of interfacial pH swings in alkaline media (pH ∼ 12.2), we measured the characteristic Raman bands for phosphate (PO_4^{3-}) and hydrogen phosphate (HPO_4^{2-}) species. As shown in Figure 2a, the PMP electrolyte prepared at p$K_{a,3}$

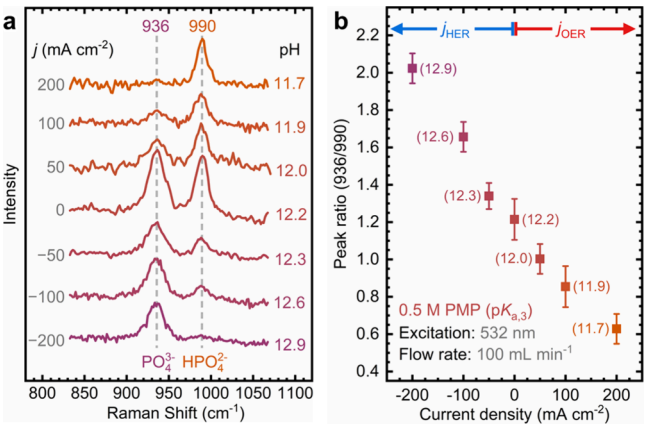

Figure 2. Local pH swings increase with applied current density in alkaline electrolyte. In-line CFRS measurements during water electrolysis using the phosphate molecular probe under alkaline conditions (p$K_{a,3}$ = 12.36): (a) Raman spectra collected at increasing OER and HER current densities, and (b) plot of the phosphate/hydrogen phosphate peak ratio as a function of the applied current density. The pH values in parentheses are estimated using the calibration curve shown in Figure S3. Data were collected with the laser beam located nominally 10 μm from the electrode surface.

exhibits two distinct Raman bands for PO_4^{3-} and HPO_4^{2-} at 936 and 990 cm^{-1}, respectively, consistent with prior observations.[35] These peaks are observed across a broad pH range (11.5−13.4, see Figure S3a), which allows their intensity ratio to be used to deduce the relative proportions of these species in solution. By measuring peak ratios in PMP electrolyte standards with adjusted pH values (Figure S3b), a calibration curve can be constructed (pH range: 9.3−13.9). This procedure allows the estimation of interfacial pH in subsequent experiments.

Figure 2b shows the PO_4^{3-}/HPO_4^{2-} peak ratios as a function of current density, with the corresponding interfacial pH derived from the calibration curve. Under OER current densities (50−200 mA·cm^{-2}), the HPO_4^{2-} peak intensity increases, indicating a lower interfacial pH. In contrast, HER current densities increase the PO_4^{3-} peak intensity, corresponding to a more alkaline interfacial pH. This trend can be further analyzed by plotting the H^+ and OH^- concentrations instead (Figure S4), revealing an exponential increase in local ion concentration with rising current density.

The observed behavior aligns with expected trends for the OER (eq 1) and HER (eq 2) in alkaline media, where hydroxide (OH^-) ions are consumed by the OER and generated by the HER:[38]

$$4OH^- \rightarrow O_2 + 2H_2O + 4e^- \quad (1)$$

$$4H_2O + 4e^- \rightarrow 2H_2 + 4OH^- \quad (2)$$

The experimental trend in Figure 2b demonstrates that interfacial pH is governed by the balance between OH^- consumption and its transport from the bulk solution. As the current density increases (reflecting higher rates of OH^- consumption or generation), ion transport struggles to keep pace with surface reaction rates, leading to more pronounced interfacial pH swings.[4,39]

To further investigate the role of ion transport in interfacial pH dynamics, Raman spectra were collected at varying distances (nominally 10, 20, 30, 40, and 50 μm, ± 2 μm) from the electrode surface. Measurements were performed at two electrolyte flow rates (50 and 100 mL·min^{-1}), with the resulting spectra shown in Figure S5. The corresponding local pH and H^+ concentration profiles are presented in Figure S6, highlighting two key findings: (1) local pH swings are more pronounced closer to the electrode surface, approaching the bulk pH as the distance increases, and (2) higher flow rates enhance ion transport, which decreases the distance required to reach bulk pH and attenuates the spatial extent of interfacial pH swings.

BULK ELECTROLYTE PH INFLUENCES THE MAGNITUDE OF LOCAL PH SWINGS

Next, we used in-line CFRS to measure the magnitude of interfacial pH swings under near-neutral conditions. Figure 3a shows Raman spectra collected at increasing current densities using a 0.5 M PMP electrolyte prepared at pH ∼ 7.4. The spectra display distinct bands for hydrogen phosphate (HPO_4^{2-}) at 989 cm^{-1} and dihydrogen phosphate ($H_2PO_4^-$) at 877 cm^{-1}.[35] A calibration curve constructed from the ratio of these peaks shows linearity within a pH range of 5.5 to 9.0 (Figure S7). As shown in Figure 3a, the intensity of the HPO_4^{2-} band decreases with increasing OER currents, while the $H_2PO_4^-$ band shows the opposite trend. After converting these spectral changes into interfacial pH values (Figure 3b), it

https://doi.org/10.1021/acsenergylett.5c00582
ACS Energy Lett. 2025, 10, 2075−2083

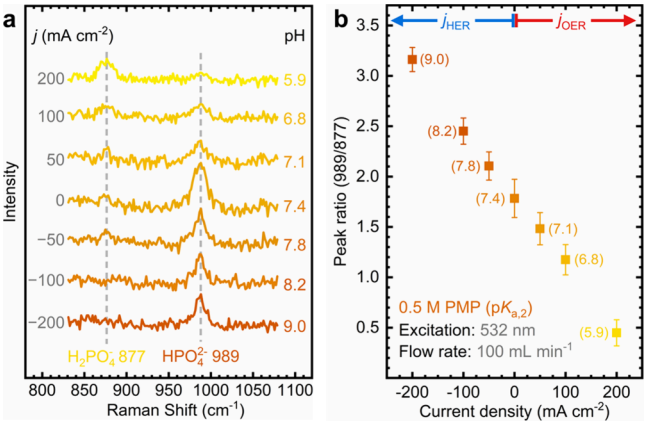

Figure 3. Local pH swings increase with applied current density in near-neutral bulk electrolyte. In-line CFRS measurements during water electrolysis using the phosphate molecular probe under near-neutral conditions ($pK_{a,2}$ = 7.20): (a) Raman spectra collected at increasing OER and HER current densities, and (b) plot of the monohydrogen phosphate/dihydrogen phosphate peak ratio as a function of the applied current density. The pH values in parentheses are estimated using the calibration curve shown in Figure S7. Data was collected with the laser beam located nominally 10 μm from the electrode surface.

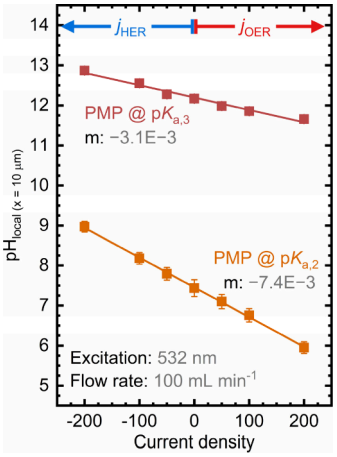

Figure 4. Local pH swings vary in magnitude depending on the bulk electrolyte pH. Local pH changes as a function of the applied current density for the in-line CFRS technique using the phosphate molecular probe under alkaline ($pK_{a,3}$ = 12.36) and near-neutral conditions ($pK_{a,2}$ = 7.20). The slope (m) was determined through a linear fit of the data measured for the phosphate molecular probe at each pK_a. Data was collected with the laser beam located nominally 10 μm from the electrode surface.

becomes evident that local pH increases with HER current densities and decreases with OER currents. Furthermore, a stark increase in the local H^+ and OH^- concentrations with increasing current densities is seen in Figure S8, reflecting the strong impact of high currents under near-neutral conditions.

In neutral and acidic electrolytes, the OER and HER follow the reactions described in eqs 3 and 4, respectively:[38]

$$2H_2O \rightarrow O_2 + 4H^+ + 4e^- \quad (3)$$

$$4H^+ + 2e^- \rightarrow 2H_2 \quad (4)$$

where protons (H^+) are generated by the OER and consumed by the HER. Consequently, the interfacial pH is dictated by the balance between H^+ consumption and transport from the bulk solution. Similar to the trends observed in alkaline media (Figure 2), the OER acidifies the interfacial microenvironment, while the HER leads to higher alkalinity.[4]

Figure 4 compares the magnitude of interfacial pH swings as a function of current density for alkaline and near-neutral conditions. Both cases exhibit a linear relationship; however, the slope is steeper under near-neutral conditions. Specifically, the local pH swing reaches nearly three pH units in neutral electrolyte, compared to nominally 1.5 pH units in alkaline media. Similarly, the Seitz group reported greater local pH changes in neutral bulk pH electrolytes during the ORR at lower current densities, using a rotating ring-disk electrode with an iridium oxide-coated Au ring as a pH probe.[10] Figure S9 provides a clearer distinction between near-neutral and alkaline conditions, especially at high current densities, when local H^+ and OH^- concentrations are plotted instead of pH. While OER currents sharply increase the local H^+ concentration in near-neutral electrolytes, HER currents increase the local OH^- concentration in alkaline media. These plots clarify quantitatively how near-neutral and alkaline electrolytes undergo pronounced interfacial pH swings depending on the reaction.

The limited buffering capacity of the PMP electrolyte, especially under near-neutral conditions, has been attributed to the depletion of ions and buffer species at the electrode–electrolyte interface by strong local pH shifts at high current densities.[39] The interfacial pH can be moderated by the supply of H^+ or OH^- ions from the bulk, which is determined by the bulk pH,[10,39] explaining why alkaline electrolytes show smaller local pH swings. The Surendranath group also showed that while buffers can attenuate local pH swings under mild polarization (i.e., −50 mA·cm^{-2}), even highly buffered neutral electrolytes cannot prevent large pH shifts at current densities beyond −100 mA·cm^{-2}.[4] Thus, local pH changes are expected to be more severe in electrolytes with low bulk H^+/OH^- concentrations and in the absence of phosphate species. Our study complements these findings and demonstrates that the bulk pH exerts a dominant influence on the magnitude of interfacial pH swings at high current densities and across varying fluid transport conditions—even in the presence of a buffer.

ONE-DIMENSIONAL ANALYSIS OF INTERFACIAL PH DYNAMICS UNDER HIGH CURRENT DENSITIES

Building on our experimental observations of interfacial pH swings, we compared these trends with theoretical models that describe local pH as a function of current density. The Nocera group proposed a straightforward model that incorporates the bulk pH, buffer composition, pK_a, and diffusion layer thickness to predict local pH swings during the OER.[39] By considering the same sets of equations and boundary conditions, we derived an expression to calculate the pH at the electrode surface (x = 0) during the HER (Section S5, Supporting Information). Figure S10 shows the interfacial pH profiles for alkaline and near-neutral conditions under HER and OER currents, as well as varying boundary layer thicknesses. In contrast to our experimental results, the model predicts a sharp pH shift once the buffer capacity is exceeded at (1) high current densities and (2) thicker boundary layers, regardless of the phosphate equilibrium's pK_a. Reducing the apparent

https://doi.org/10.1021/acsenergylett.5c00582
ACS Energy Lett. 2025, 10, 2075−2083

boundary layer to 10 μm results in less pronounced pH swings and a linear response to the applied current density.

Although the Nocera pH model effectively captures general trends in interfacial pH swings, its quantitative limitations stem from considering only a single pK_a (the phosphate equilibrium involves three pK_a values) and neglecting buffer reaction kinetics. To address these gaps, we developed a one-dimensional continuum model using COMSOL Multiphysics to estimate interfacial pH swings (Section S6, Supporting Information). Figure S11 shows predicted interfacial pH profiles (x = 0) across various current densities and boundary layer thicknesses. The continuum model also enables the estimation of local pH at fixed distances from the electrode. Figure S12 shows local pH profiles at varying current densities at x = 10 μm to enable direct comparison with our experimental CFRS measurements. The continuum pH model corroborates that interfacial pH swings are more pronounced under near-neutral pH and reveals that the local pH profiles at x = 10 μm deviate significantly from that at the electrode surface.

To exploit this capability of the continuum model, we plotted local pH as a function of distance from the electrode surface for alkaline (Figure S13) and near-neutral (Figure S14) conditions under two boundary layer thicknesses (corresponding to experimental CFRS flow rates). These profiles confirm two trends: (1) local pH swings are more significant near the electrode surface and attenuate with distance, and (2) thinner boundary layers, resulting from faster flow rates, mitigate pH swings. Combining insights from the Nocera pH model, COMSOL simulations, and our experimental CFRS data, we conclude that interfacial pH changes can be minimized by increasing the diffusive flux of H^+ and OH^- from the bulk via two strategies: (1) reducing boundary layer thickness through improved mixing, which shortens ion transport paths, and (2) increasing bulk ion concentrations (e.g., highly acidic or alkaline conditions). These findings underscore how stagnant and dilute electrolytes are particularly susceptible to pronounced interfacial pH swings, necessitating caution and proactive countermeasures in such systems.

A notable discrepancy between our experimental CFRS results and theoretical pH models arises at high current densities (>100 mA·cm^{-2}) and thicker boundary layers (>20 μm), where models predict nonlinear profiles due to limited ion transport. This deviation is apparent when local pH profiles at a 30 μm boundary layer are overlapped (Figure S15), especially under near-neutral pH. Better agreement between predictions and experiments is observed when assuming a thinner apparent boundary layer (δ = 23 μm), as shown in Figure 5. Corresponding local H^+ and OH^- concentrations also show better agreement when plotted instead of pH (Figure S16).

This thinner apparent boundary layer could result from processes not captured by the ferricyanide reduction method used to characterize mass transport—specifically, bubble evolution during water electrolysis. Hydrogen and oxygen gases, produced by the HER and OER, respectively, form bubbles once their solubility limit is exceeded. The formation, coalescence, and detachment of gas bubbles agitate the electrolyte and disrupt the stagnant boundary layer, thereby enhancing mass transport.[31,40,41] Moreover, the dynamic behavior of bubbles can induce localized convection and even cavitation effects that further impact the electrode–electrolyte interface and the boundary layer.[31,42] This finding

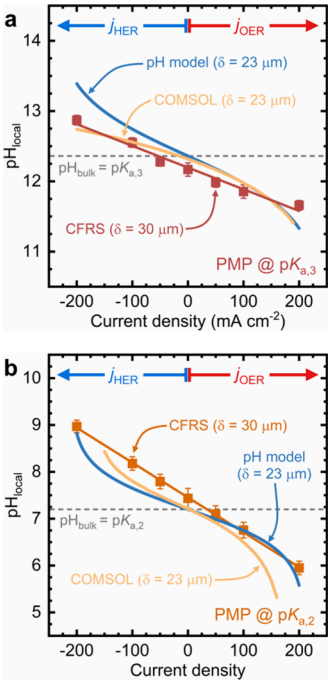

Figure 5. Experimental pH swings from in-line CFRS match theoretical models with thinner boundary layers. Magnitude of local pH changes as a function of the applied current density for the phosphate molecular probe at (a) p$K_{a,3}$ and (b) p$K_{a,2}$. Experimental results from in-line CFRS are contrasted with local pH profiles derived from the Nocera and our continuum models. The boundary layer thickness (δ) is shown in parentheses. Local pH values were calculated at 10 μm from the electrode surface for the experimental CFRS technique and our continuum model. Local pH values for the Nocera pH model were calculated at the electrode surface (x = 0). The horizontal dashed line shows the bulk pH for the PMP electrolyte at its pK_a as a reference.

suggests that redox couples fail to reliably estimate boundary layer thickness in gas-evolving systems, highlighting the need for more suitable methods to measure it. In line with previous evidence,[41] we hypothesize that bubble evolution at high current densities increases ion flux from the bulk electrolyte to the electrode surface. This enhanced transport could attenuate local pH swings, resulting in the linear profiles observed experimentally. These CFRS findings motivate future studies to experimentally control and exploit bubble evolution (e.g., by modifying the electrode morphology, hydrophilicity/hydrophobicity, etc.) to impact interfacial pH swings in a desirable manner.[42]

IN-LINE CFRS METHOD VALIDATION AND APPLICABILITY

We conducted a series of systematic control experiments to demonstrate the capabilities of the in-line CFRS method for quantifying local pH swings. These are detailed in the Supporting Information, including figures, tables, and explanatory notes describing the procedures and their significance.

We first evaluated the method's applicability in various near-neutral and alkaline electrolytes (Figure S17). The key difference among these electrolytes lies in their ion conduction resistance, estimated from the high-frequency resistance (Table S4). After correcting for the ohmic drop in the polarization curves, more alkaline electrolytes (e.g., 1 M KOH) showed lower cell potentials, consistent with reduced OH^- concen-

https://doi.org/10.1021/acsenergylett.5c00582
ACS Energy Lett. 2025, 10, 2075−2083

tration overpotentials at higher pH.[43] It is important to note that adding 0.5 M PMP does not affect water-splitting kinetics, as shown by the nearly identical polarization curves for 1 M KOH with and without PMP. Although phosphate buffers are known to impact mass transport and concentration overpotentials,[43−47] our in-line CFRS method operates under (1) higher current densities than most previous studies (typically ∼10 mA·cm^{-2}), (2) more dilute PMP concentrations (compared to values up to 4 M), and (3) forced flow to enhance mass transport. Our results also suggest that mass transport enhancement due to gas bubble evolution plays a significant role—likely greater than pH buffers. Collectively, these findings indicate that under high current densities and enhanced mass transport, the effect of phosphate on electrochemical performance and buffering capacity may be diminished. Still, further studies are needed to elucidate the specific contributions of these processes.

Next, we evaluated the signal-to-noise ratio (SNR), the limit of detection (LOD), and the limit of quantitation (LOQ) for 0.5 M PMP electrolytes (Figure S18 and Tables S5 and S6), as well as PMP-containing KOH and K_2CO_3 electrolytes (Figure S19 and Tables S7 and S8). The in-line CFRS method, when used with 0.5 M PMP, distinguishes Raman signals from background noise, with SNR values ranging from 3 to 20. While the method shows limitations in highly alkaline conditions (e.g., 1 M KOH), where the HPO_4^{2-} peak is no longer detectable, it remains effective for systems exhibiting pH swings below ∼13.3, such as carbonate-containing electrolytes (bulk pH ∼ 12). This feature represents an advantage for studying pH swings in CO_2RR,[7,41] as the CO_3^{2-} band is not obscured by PO_4^{3-}/HPO_4^{2-} signals, allowing interfacial pH to be measured up to ∼13.3.

We emphasize the importance of optimizing operating conditions to improve the method's analytical performance. Increasing the concentration of the PMP electrolyte maximizes the SNR, with 0.1 M identified as the lowest concentration that still meets the recommended threshold (Figure S20 and Tables S9 and S10). Increasing the flow rate also improves the SNR (Figure S21 and Tables S11 and S12). The method performs poorly under stagnant conditions, where gas bubbles accumulate on the electrode surface and interfere with detection. Thus, an optimal electrolyte flow is essential for removing gas bubbles during in-line CFRS measurements (Figure S21c).

Local pH changes occur in less than 10 s—the shortest acquisition time that still produced clear Raman signals—and remain stable over time (Figure S22). This behavior is consistent with previous findings showing that pH swings occur within 1−2 s under high currents.[4] Additionally, alternating current experiments confirm that local pH swings are reversible, with shifts occurring on the same electrode by simply switching the current polarity (Figure S23). These results reveal the highly dynamic and rapid nature of interfacial pH changes, emphasizing that their effects on electrochemical interfaces can arise over very short time scales.

Our in-line CFRS technique allows for statistically confident pH quantification above ±50 mA·cm^{-2}, with visible but less significant changes at ±25 mA·cm^{-2} (Figure S24). Although no significant pH variation was detected along the electrode surface over a 100 μm range (Figure S25), we anticipate that rougher surfaces or structural defects could lead to local pH variations and uneven bubble formation.[42] Studies on location-dependent pH gradients in larger cell architectures and other electrode geometries would be highly valuable.[19,27]

Our findings highlight in a quantitative manner how local pH differs significantly from the bulk pH in electrochemical energy conversion devices across a range of conditions. Our measurements show that interfacial pH is highly sensitive to bulk pH and operating current density. We confirm that pH swings observed in prior studies at low current densities are intensified at high current densities. Consistent with previous studies,[48] these pH swings are particularly dramatic in near-neutral conditions, even in the presence of a buffer. Results also highlight the impact of cell architecture and mass transfer on interfacial pH. We show that mass transfer influences the spatial extent and magnitude of pH swings, underscoring the need to assess cell hydrodynamics in electrochemical studies.[27] Differences in interfacial pH unintentionally introduced from variations in cell hydrodynamics may result in differences in reported catalytic activity and stability.[14] Similarly, ionomer overlayers restricting ion migration may intensify local pH gradients and influence measured results.[4] Collectively, these findings reinforce the importance of characterizing interfacial pH and the need to account for its effects in energy conversion technologies.[49]

Developing robust analytical platforms to probe electrode−electrolyte interfaces in real-time is crucial for advancing our understanding of the dynamic processes underpinning electrochemical energy conversion technologies. We have contributed to this effort by developing a spectroelectrochemical technique capable of tracking interfacial pH swings during water electrolysis. To build on previous efforts, we demonstrate the applicability of this approach under high current densities and controlled flow conditions while providing spatially resolved measurements of pH swings near the electrode surface. Our findings highlight the role of key parameters, such as the bulk electrolyte pH and cell hydrodynamics, in shaping the magnitude of these pH dynamics. Additionally, we make our cell design available for the community to encourage researchers to leverage this approach to study other PCET processes (Section S2, Supporting Information).

We envision that analytical platforms like in-line CFRS hold substantial potential for interrogating electrochemical interfaces. Future studies measuring interfacial pH swings in complex environments—such as membrane−electrode assemblies, gas diffusion layers, and porous electrodes—would greatly benefit the field.[4,41] Likewise, spin-off investigations into the effects of spectator ions,[10,50] chelation of dissolved impurities,[17,51] and bubble dynamics could offer further valuable insights.[31] Our findings can also provide insight into the role of interfacial pH in processes relevant to industrial electrolyzers, including catalyst corrosion driven by local environment effects,[52,53] buffering by gas bubbles,[41] ionomer stability,[32] and gas evolution behavior—which plays a critical role in gas crossover and shunt currents.[54−56] Translating these analytical platforms to more specialized and industrially relevant settings will accelerate the development of more efficient electrochemical energy conversion technologies.

■ ASSOCIATED CONTENT

Supporting Information

The Supporting Information is available free of charge at https://pubs.acs.org/doi/10.1021/acsenergylett.5c00582.

https://doi.org/10.1021/acsenergylett.5c00582
ACS Energy Lett. 2025, 10, 2075−2083

Experimental details regarding the in-line CFRS technique, analytical pH models, and supporting figures, tables, and schemes (PDF)

AUTHOR INFORMATION

Corresponding Author

C. Buddie Mullins − *Department of Chemistry, The University of Texas at Austin, Austin, Texas 78712, United States; McKetta Department of Chemical Engineering, Texas Materials Institute, Allen J. Bard Center for Electrochemistry, and H2@UT, The University of Texas at Austin, Austin, Texas 78712, United States;* orcid.org/0000-0003-1030-4801; Email: mullins@che.utexas.edu

Authors

Raul A. Marquez − *Department of Chemistry, The University of Texas at Austin, Austin, Texas 78712, United States;* orcid.org/0000-0003-3885-5007

Jay T. Bender − *McKetta Department of Chemical Engineering, The University of Texas at Austin, Austin, Texas 78712, United States*

Shashwati C. da Cunha − *McKetta Department of Chemical Engineering, The University of Texas at Austin, Austin, Texas 78712, United States;* orcid.org/0009-0002-2149-1702

Ashton M. Aleman − *Department of Chemical Engineering, Stanford University, Stanford, California 94305, United States; SUNCAT Center for Interface Science and Catalysis, SLAC National Accelerator Laboratory, Menlo Park, California 94025, United States;* orcid.org/0000-0003-4698-2807

Amaresh Sahu − *McKetta Department of Chemical Engineering, The University of Texas at Austin, Austin, Texas 78712, United States*

Venkat Ganesan − *McKetta Department of Chemical Engineering, The University of Texas at Austin, Austin, Texas 78712, United States;* orcid.org/0000-0003-3899-5843

Delia J. Milliron − *Department of Chemistry, The University of Texas at Austin, Austin, Texas 78712, United States; McKetta Department of Chemical Engineering, Allen J. Bard Center for Electrochemistry, and H2@UT, The University of Texas at Austin, Austin, Texas 78712, United States;* orcid.org/0000-0002-8737-451X

Joaquin Resasco − *McKetta Department of Chemical Engineering and H2@UT, The University of Texas at Austin, Austin, Texas 78712, United States;* orcid.org/0000-0001-6374-9877

Thomas F. Jaramillo − *Department of Chemical Engineering, Stanford University, Stanford, California 94305, United States; SUNCAT Center for Interface Science and Catalysis, SLAC National Accelerator Laboratory, Menlo Park, California 94025, United States;* orcid.org/0000-0001-9900-0622

Complete contact information is available at: https://pubs.acs.org/10.1021/acsenergylett.5c00582

Author Contributions

R.A.M.: Conceptualization, Methodology, Formal analysis, Investigation, Writing − original draft, Visualization. **J.T.B.**: Conceptualization, Investigation, Formal analysis, Writing − review and editing. **S.C.d.C.**: Conceptualization, Investigation, Methodology, Writing − review and editing. **A.M.A.**: Conceptualization, Writing − review and editing. **A.S.**: Conceptualization. **V.G.**: Conceptualization. **D.J.M.**: Resources, Writing − review and editing, Supervision, Funding acquisition. **J.R.**: Conceptualization, Writing − review and editing, Supervision, Funding acquisition. **T.F.J.**: Conceptualization, Resources, Writing − review and editing, Supervision, Funding acquisition. **C.B.M.**: Conceptualization, Resources, Writing − review and editing, Project administration, Funding acquisition. All authors have approved the final version of the manuscript.

Notes

The authors declare no competing financial interest.

ACKNOWLEDGMENTS

The authors gratefully acknowledge funding from the National Science Foundation (NSF) via Grant CHE-2102307 and the Welch Foundation through Grants F-2076, F-1599, F-2208, and F-1848 for their generous support. D.J.M. and J.R. acknowledge support from the UT Austin Energy Institute. A.M.A. and T.F.J. were supported by the U.S. Department of Energy, Office of Science, Office of Basic Energy Sciences, Chemical Sciences, Geosciences, and Biosciences Division, Catalysis Science Program to the SUNCAT Center for Interface Science and Catalysis for contributions to the experimental design and analysis. R.A.M. acknowledges CONAHCYT for his Doctoral Scholarship Award (CVU 919871) and the generous support from the Electrochemical Society through the 2024 Edward G. Weston Summer Fellowship. We thank David Gray and Shallaco McDonald for manufacturing the flow cell for CFRS measurements.

REFERENCES

(1) Schreier, M.; Kenis, P.; Che, F.; Hall, A. S. Trends in Electrocatalysis: The Microenvironment Moves to Center Stage. *ACS Energy Lett.* **2023**, *8* (9), 3935−3940.

(2) Lucky, C.; Schreier, M. Mind the Interface: The Role of Adsorption in Electrocatalysis. *ACS Nano* **2024**, *18* (8), 6008−6015.

(3) Li, X.; Zhu, W.; Zhang, Y.; Zhao, Y.; Wang, D.; Zhen, Y.; Fu, F.; Yang, C. Rational Design of Local Microenvironment for Electrocatalytic Water Splitting. *Inorg. Chem. Front.* **2024**, *11* (14), 4080−4106.

(4) Sauvé, E. R.; Tang, B. Y.; Razdan, N. K.; Toh, W. L.; Weng, S.; Surendranath, Y. Open Circuit Potential Decay Transients Quantify Interfacial pH Swings during High Current Density Hydrogen Electrocatalysis. *Joule* **2024**, *8* (3), 728−745.

(5) Böhme, A.; Bui, J. C.; Fenwick, A. Q.; Bhide, R.; Feltenberger, C. N.; Welch, A. J.; King, A. J.; Bell, A. T.; Weber, A. Z.; Ardo, S.; Atwater, H. A. Direct Observation of the Local Microenvironment in Inhomogeneous CO_2 Reduction Gas Diffusion Electrodes via Versatile pOH Imaging. *Energy Environ. Sci.* **2023**, *16* (4), 1783−1795.

(6) Govindarajan, N.; Xu, A.; Chan, K. How pH Affects Electrochemical Processes. *Science* **2022**, *375* (6579), 379−380.

(7) Zhang, Z.; Melo, L.; Jansonius, R. P.; Habibzadeh, F.; Grant, E. R.; Berlinguette, C. P. pH Matters When Reducing CO_2 in an Electrochemical Flow Cell. *ACS Energy Lett.* **2020**, *5* (10), 3101−3107.

(8) Varela, A. S.; Kroschel, M.; Reier, T.; Strasser, P. Controlling the Selectivity of CO_2 Electroreduction on Copper: The Effect of the Electrolyte Concentration and the Importance of the Local pH. *Catal. Today* **2016**, *260*, 8−13.

(9) Duan, Z.; Henkelman, G. Theoretical Resolution of the Exceptional Oxygen Reduction Activity of Au(100) in Alkaline Media. *ACS Catal.* **2019**, *9* (6), 5567−5573.

(10) Ruggiero, B. N.; Sanroman Gutierrez, K. M.; George, J. D.; Mangan, N. M.; Notestein, J. M.; Seitz, L. C. Probing the Relationship

between Bulk and Local Environments to Understand Impacts on Electrocatalytic Oxygen Reduction Reaction. *J. Catal.* **2022**, *414*, 33−43.
(11) Kelly, S. R.; Kirk, C.; Chan, K.; Nørskov, J. K. Electric Field Effects in Oxygen Reduction Kinetics: Rationalizing pH Dependence at the Pt(111), Au(111), and Au(100) Electrodes. *J. Phys. Chem. C* **2020**, *124* (27), 14581−14591.
(12) Yang, C.; Batuk, M.; Jacquet, Q.; Rousse, G.; Yin, W.; Zhang, L.; Hadermann, J.; Abakumov, A. M.; Cibin, G.; Chadwick, A.; Tarascon, J.-M.; Grimaud, A. Revealing pH-Dependent Activities and Surface Instabilities for Ni-Based Electrocatalysts during the Oxygen Evolution Reaction. *ACS Energy Lett.* **2018**, *3* (12), 2884−2890.
(13) Yan, K.; Lee, S.-W.; Yap, K. M. K.; Mule, A. S.; Hannagan, R. T.; Matthews, J. E.; Kamat, G. A.; Lee, D. U.; Stevens, M. B.; Nielander, A. C.; Jaramillo, T. F. On-Line Inductively Coupled Plasma Mass Spectrometry Reveals Material Degradation Dynamics of Au and Cu Catalysts during Electrochemical CO_2 Reduction. *J. Am. Chem. Soc.* **2025**, *147* (5), 4079−4088.
(14) Geuß, M.; Löttert, L.; Böhm, T.; Hutzler, A.; Mayrhofer, K. J. J.; Thiele, S.; Cherevko, S. Quantification of Iridium Dissolution at Water Electrolysis Relevant Conditions Using a Gas Diffusion Electrode Half-Cell Setup. *ACS Catal.* **2024**, *14* (15), 11819−11831.
(15) Yap, K. M. K.; Wei, W. J.; Pabón, M. R.; King, A. J.; Bui, J. C.; Wei, L.; Lee, S.-W.; Weber, A. Z.; Bell, A. T.; Nielander, A. C.; Jaramillo, T. F. Modeling Diurnal and Annual Ethylene Generation from Solar-Driven Electrochemical CO_2 Reduction Devices. *Energy Environ. Sci.* **2024**, *17*, 2453−2467.
(16) Márquez, R. A.; Kawashima, K.; Son, Y. J.; Castelino, G.; Miller, N.; Smith, L. A.; Chukwuneke, C. E.; Mullins, C. B. Getting the Basics Right: Preparing Alkaline Electrolytes for Electrochemical Applications. *ACS Energy Lett.* **2023**, *8* (2), 1141−1146.
(17) Wuttig, A.; Surendranath, Y. Impurity Ion Complexation Enhances Carbon Dioxide Reduction Catalysis. *ACS Catal.* **2015**, *5* (7), 4479−4484.
(18) Marquez, R. A.; Espinosa, M.; Kalokowski, E.; Son, Y. J.; Kawashima, K.; Le, T. V.; Chukwuneke, C. E.; Mullins, C. B. A Guide to Electrocatalyst Stability Using Lab-Scale Alkaline Water Electrolyzers. *ACS Energy Lett.* **2024**, *9* (2), 547−555.
(19) Obata, K.; van de Krol, R.; Schwarze, M.; Schomacker, R.; Abdi, F. F. In Situ Observation of pH Change during Water Splitting in Neutral pH Conditions: Impact of Natural Convection Driven by Buoyancy Effects. *Energy Environ. Sci.* **2020**, *13* (12), 5104−5116.
(20) Monteiro, M. C. O.; Mirabal, A.; Jacobse, L.; Doblhoff-Dier, K.; Barton, S. C.; Koper, M. T. M. Time-Resolved Local pH Measurements during CO_2 Reduction Using Scanning Electrochemical Microscopy: Buffering and Tip Effects. *JACS Au* **2021**, *1* (11), 1915−1924.
(21) Albery, W. J.; Calvo, E. J. Ring-Disc Electrodes. Part 21.—pH Measurement with the Ring. *J. Chem. Soc., Faraday Trans. 1* **1983**, *79* (11), 2583−2596.
(22) Liu, H.; Yan, T.; Tan, S.; Sun, L.; Zhang, Z.; Hu, S.; Li, S.-H.; Kang, X.; Lei, Y.; Jiang, L.; Hou, T.; Liu, L.; Yu, Q.; Liu, B. Observation on Microenvironment Changes of Dynamic Catalysts in Acidic CO_2 Reduction. *J. Am. Chem. Soc.* **2024**, *146* (8), 5333−5342.
(23) Ayemoba, O.; Cuesta, A. Spectroscopic Evidence of Size-Dependent Buffering of Interfacial pH by Cation Hydrolysis during CO_2 Electroreduction. *ACS Appl. Mater. Interfaces* **2017**, *9* (33), 27377−27382.
(24) Zheng, X.; Shi, X.; Ning, H.; Yang, R.; Lu, B.; Luo, Q.; Mao, S.; Xi, L.; Wang, Y. Tailoring a Local Acid-like Microenvironment for Efficient Neutral Hydrogen Evolution. *Nat. Commun.* **2023**, *14* (1), 4209.
(25) Xie, Z.; Wang, Q.; Yang, R.; Zhang, J.; Ou, S.; Ouyang, G.; Li, M.; Shi, J.; Tong, Y. In-Situ Imaging and Time-Resolved Investigation of Local pH in Electrocatalytic CO_2 Reduction. *Appl. Catal. B Environ.* **2025**, *362*, 124727.
(26) Zheng, W. Beginner's Guide to Raman Spectroelectrochemistry for Electrocatalysis Study. *Chemistry-Methods* **2023**, *3*, No. e202200042.
(27) Márquez-Montes, R. A.; Collins-Martínez, V. H.; Pérez-Reyes, I.; Chávez-Flores, D.; Graeve, O. A.; Ramos-Sánchez, V. H. Electrochemical Engineering Assessment of a Novel 3D-Printed Filter-Press Electrochemical Reactor for Multipurpose Laboratory Applications. *ACS Sustain. Chem. Eng.* **2020**, *8* (9), 3896−3905.
(28) Alia, S. M.; Reeves, K. S.; Cullen, D. A.; Yu, H.; Kropf, A. J.; Kariuki, N.; Park, J. H.; Myers, D. J. Simulated Start-Stop and the Impact of Catalyst Layer Redox on Degradation and Performance Loss in Low-Temperature Electrolysis. *J. Electrochem. Soc.* **2024**, *171* (4), 044503.
(29) Aleman, A. M.; Crago, C. F.; Kamat, G. A.; Mule, A. S.; Avilés Acosta, J. E.; Matthews, J. E.; Keyes, N.; Hannagan, R. T.; Nielander, A. C.; Stevens, M. B.; Jaramillo, T. F. Multimodal In Situ Characterization Uncovers Unexpected Stability of a Cobalt Electrocatalyst for Acidic Sustainable Energy Technologies. *J. Am. Chem. Soc.* **2025**, *147* (12), 10309−10319.
(30) Du, L.; Zheng, W. Catalyst Deactivation during Water Electrolysis: Understanding and Mitigation. *APL Energy* **2024**, *2* (2), 021501.
(31) Zhao, X.; Ren, H.; Luo, L. Gas Bubbles in Electrochemical Gas Evolution Reactions. *Langmuir* **2019**, *35* (16), 5392−5408.
(32) Lindquist, G. A.; Gaitor, J. C.; Thompson, W. L.; Brogden, V.; Noonan, K. J. T.; Boettcher, S. W. Oxidative Instability of Ionomers in Hydroxide-Exchange-Membrane Water Electrolyzers. *Energy Environ. Sci.* **2023**, *16* (10), 4373−4387.
(33) Arenas, L. F.; Ponce de León, C.; Walsh, F. C. 3D-Printed Porous Electrodes for Advanced Electrochemical Flow Reactors: A Ni/Stainless Steel Electrode and Its Mass Transport Characteristics. *Electrochem. Commun.* **2017**, *77*, 133−137.
(34) Recio, F. J.; Herrasti, P.; Vazquez, L.; Ponce de León, C.; Walsh, F. C. Mass Transfer to a Nanostructured Nickel Electrodeposit of High Surface Area in a Rectangular Flow Channel. *Electrochim. Acta* **2013**, *90*, 507−513.
(35) Lu, S.; Zhang, Z.; Zhang, B.; Shi, Y. Insight into the Change in Local pH near the Electrode Surface Using Phosphate Species as the Probe. *J. Phys. Chem. Lett.* **2023**, *14* (46), 10457−10462.
(36) Kucernak, A. R.; Wang, H.; Lin, X. Avoid Using Phosphate Buffered Saline (PBS) as an Electrolyte for Accurate OER Studies. *ACS Energy Lett.* **2024**, *9* (8), 3939−3946.
(37) Lackey, H. E.; Nelson, G. L.; Lines, A. M.; Bryan, S. A. Reimagining pH Measurement: Utilizing Raman Spectroscopy for Enhanced Accuracy in Phosphoric Acid Systems. *Anal. Chem.* **2020**, *92* (8), 5882−5889.
(38) Shih, A. J.; Monteiro, M. C. O.; Dattila, F.; Pavesi, D.; Philips, M.; da Silva, A. H. M.; Vos, R. E.; Ojha, K.; Park, S.; van der Heijden, O.; Marcandalli, G.; Goyal, A.; Villalba, M.; Chen, X.; Gunasooriya, G. T. K. K.; McCrum, I.; Mom, R.; López, N.; Koper, M. T. M. Water Electrolysis. *Nat. Rev. Methods Primers* **2022**, *2* (1), 1−19.
(39) Veroneau, S. S.; Hartnett, A. C.; Ryu, J.; Hong, H.; Costentin, C.; Nocera, D. G. A Straightforward Model for Quantifying Local pH Gradients Governing the Oxygen Evolution Reaction. *J. Am. Chem. Soc.* **2024**, *146* (42), 28925−28931.
(40) Yang, X.; Baczyzmalski, D.; Cierpka, C.; Mutschke, G.; Eckert, K. Marangoni Convection at Electrogenerated Hydrogen Bubbles. *Phys. Chem. Chem. Phys.* **2018**, *20* (17), 11542−11548.
(41) Baumgartner, L. M.; Kahn, A.; Hoogland, M.; Bleeker, J.; Jager, W. F.; Vermaas, D. A. Direct Imaging of Local pH Reveals Bubble-Induced Mixing in a CO_2 Electrolyzer. *ACS Sustainable Chem. Eng.* **2023**, *11* (28), 10430−10440.
(42) Márquez, R. A.; Kawashima, K.; Son, Y. J.; Rose, R.; Smith, L. A.; Miller, N.; Carrasco Jaim, O. A.; Celio, H.; Mullins, C. B. Tailoring 3D-Printed Electrodes for Enhanced Water Splitting. *ACS Appl. Mater. Interfaces* **2022**, *14* (37), 42153−42170.
(43) Shinagawa, T.; Takanabe, K. Electrocatalytic Hydrogen Evolution under Densely Buffered Neutral pH Conditions. *J. Phys. Chem. C* **2015**, *119* (35), 20453−20458.
(44) Shinagawa, T.; Takanabe, K. Electrolyte Engineering toward Efficient Hydrogen Production Electrocatalysis with Oxygen-Cross-

https://doi.org/10.1021/acsenergylett.5c00582
ACS Energy Lett. 2025, 10, 2075−2083

over Regulation under Densely Buffered Near-Neutral pH Conditions. *J. Phys. Chem. C* **2016**, *120* (3), 1785−1794.
(45) Shinagawa, T.; Ng, M. T.-K.; Takanabe, K. Electrolyte Engineering towards Efficient Water Splitting at Mild pH. *ChemSusChem* **2017**, *10* (21), 4155−4162.
(46) Naito, T.; Shinagawa, T.; Nishimoto, T.; Takanabe, K. Water Electrolysis in Saturated Phosphate Buffer at Neutral pH. *ChemSusChem* **2020**, *13* (22), 5921−5933.
(47) Shinagawa, T.; Takanabe, K. Towards Versatile and Sustainable Hydrogen Production through Electrocatalytic Water Splitting: Electrolyte Engineering. *ChemSusChem* **2017**, *10* (7), 1318−1336.
(48) Yang, K.; Kas, R.; Smith, W. A. In Situ Infrared Spectroscopy Reveals Persistent Alkalinity near Electrode Surfaces during CO_2 Electroreduction. *J. Am. Chem. Soc.* **2019**, *141* (40), 15891−15900.
(49) Resasco, J.; Lum, Y.; Clark, E.; Zeledon, J. Z.; Bell, A. T. Effects of Anion Identity and Concentration on Electrochemical Reduction of CO_2. *ChemElectroChem.* **2018**, *5* (7), 1064−1072.
(50) Bender, J. T.; Petersen, A. S.; Østergaard, F. C.; Wood, M. A.; Heffernan, S. M. J.; Milliron, D. J.; Rossmeisl, J.; Resasco, J. Understanding Cation Effects on the Hydrogen Evolution Reaction. *ACS Energy Lett.* **2023**, *8* (1), 657−665.
(51) Marquez, R. A.; Kalokowski, E.; Espinosa, M.; Bender, J. T.; Son, Y. J.; Kawashima, K.; Chukwuneke, C. E.; Smith, L. A.; Celio, H.; Dolocan, A.; Zhan, X.; Miller, N.; Milliron, D. J.; Resasco, J.; Mullins, C. B. Transition Metal Incorporation: Electrochemical, Structure, and Chemical Composition Effects on Nickel Oxyhydroxide Oxygen-Evolution Electrocatalysts. *Energy Environ. Sci.* **2024**, *17* (5), 2028−2045.
(52) Marquez, R. A.; Oefelein, E. E.; Le, T. V.; Kawashima, K.; Smith, L. A.; Mullins, C. B. Redefining the Stability of Water Oxidation Electrocatalysts: Insights from Materials Databases and Machine Learning. *ACS Materials Lett.* **2024**, *6*, 2905−2918.
(53) Komiya, H.; Obata, K.; Honma, T.; Takanabe, K. Dynamic Stabilization of Nickel-Based Oxygen Evolution Electrocatalysts in the Presence of Chloride Ions Using a Phosphate Additive. *J. Mater. Chem. A* **2024**, *12* (6), 3513−3522.
(54) Lira Garcia Barros, R.; Kelleners, M. H. G.; van Bemmel, L.; van der Leegte, T. V. N.; van der Schaaf, J.; de Groot, M. T. Elucidating the Increased Ohmic Resistances in Zero-Gap Alkaline Water Electrolysis. *Electrochim. Acta* **2024**, *507*, 145161.
(55) Lira Garcia Barros, R.; Kraakman, J. T.; Sebregts, C.; van der Schaaf, J.; de Groot, M. T. Impact of an Electrode-Diaphragm Gap on Diffusive Hydrogen Crossover in Alkaline Water Electrolysis. *Int. J. Hydrogen Energy* **2024**, *49*, 886−896.
(56) Rasten, E. (Invited) Shunt-Currents in Alkaline Water-Electrolyzers and Renewable Energy. *ECS Trans.* **2024**, *113* (9), 25−41.

https://doi.org/10.1021/acsenergylett.5c00582
ACS Energy Lett. 2025, 10, 2075−2083